HHS Public Access

Author manuscript

*Biomaterials*. Author manuscript; available in PMC 2019 June 04.

Published in final edited form as:

*Biomaterials*. 2012 November ; 33(31): 7785–7793. doi:10.1016/j.biomaterials.2012.07.022.

# PET imaging of tumor associated macrophages using mannose coated $^{64}$Cu liposomes

**Landon W. Locke**[a], **Marty W. Mayo**[b], **Alexander D. Yoo**[c], **Mark B. Williams**[a,d,e], and **Stuart S. Berr**[a,d,*]

[a]Department of Biomedical Engineering, The University of Virginia, PO Box 801339, 480 Ray C Hunt Drive, Charlottesville, VA 22908, USA

[b]Department of Biochemistry and Molecular Genetics, The University of Virginia, PO Box 800733, Charlottesville, VA 22908, USA

[c]The School of Medicine, The University of Virginia, Charlottesville, VA 22908, USA

[d]Department of Radiology and Medical Imaging, The University of Virginia, PO Box 801332, 480 Ray C Hunt Drive, Charlottesville, VA 22908, USA

[e]Department of Physics, The University of Virginia, Charlottesville, VA 22908, USA

## Abstract

Macrophages within the tumor microenvironment (TAMs) have been shown to play a major role in the growth and spread of many types of cancer. Cancer cells produce cytokines that cause macrophages to express scavenger receptors (e.g. the mannose receptor) and factors that facilitate tissue and blood vessel growth, suppress T cell mediated anti-tumor activity, and express enzymes that can break down the extracellular matrix, thereby promoting metastasis. We have designed a mannosylated liposome (MAN-LIPs) and show that it accumulates in TAMs in a mouse model of pulmonary adenocarcinoma. These liposomes are loaded with $^{64}$Cu to allow tracking by PET imaging, and contain a fluorescent dye in the lipid bilayer permitting subsequent fluorescence microscopy. We injected these liposomes into a mouse model of lung cancer. *In vivo* PET images were acquired 6 h after injection followed by the imaging of select excised organs. MAN-LIPs accumulated in TAMs and exhibited little accumulation in remote lung areas. MAN-LIPs are a promising new vehicle for the delivery of imaging agents to lung TAMs. In addition to imaging, MAN-LIPs hold the potential for delivery of therapeutic agents to the tumor microenvironment.

### Keywords

Animal model; Liposome; Macrophage; Molecular imaging; Positron emission tomography

*Corresponding author. 480 Ray C. Hunt Drive, Room 157, Sheridan G. Snyder Translational Research Building, University of Virginia, USA. Tel.: +1 434 924 5096; fax: +1 434 982 4129., berr@virginia.edu (S.S. Berr).

## 1. Introduction

Macrophages participate centrally in many pulmonary diseases. In addition to their elevated presence in the lungs of COPD [1] and CF [2] patients, evidence has emerged linking macrophages to the development/progression of lung tumors [3,4]. Enhancing cell survival, promoting tissue remodeling, angiogenesis, and suppressing the antitumor adaptive immune response are all protumor functions of tumor associated macrophages (TAMs) [3–6]. In animal studies, the depletion or blockade of TAMs into the tumor microenvironment (TME) has been shown to inhibit tumor growth and reduce tumor vessel density [7–9]. Clinical data have shown that TAMs are present in high density in many human tumors, including lung, breast, skin, and prostate. Furthermore, their presence and density correlates with cancer invasion and decreased patient survival time [4,10,11]. The macrophage (MØ) subtype strongly influences its interaction with the tumor. The M2 subtype is found to facilitate tumor growth, while the M1 subtype impedes it, although exceptions to this generalization have been reported. TAMs represent a unique target for cancer therapies.

As a result of these observations, methods for monitoring TAMs *in vivo* are currently being explored to help better understand their role in lung tumor promotion and for assessing macrophage-targeted therapies. Molecular imaging using agents targeted to TAMs offers a noninvasive and quantitative method for assessing the presence and density of these cells. Some progress has been made in this area. A dextran-coated magneto-fluorescent nanoparticle decorated with the amino acid glycine (CLIO-gly) was reported to accumulate in TAMs [12]. It also was shown that the agent could successfully track the depletion of TAMs following the administration of liposomal clodronate [13]. Another agent, poly(L-glutamic acid)-Gd-chelated *p*-aminobenzyl-diethylenetriaminepentaacetic acid (PG-Gd-NIR813), was reported to label TAMs *in vivo* [14]. The mechanism of uptake of CLIO-gly and PG-Gd-NIR813 by TAMs is currently undetermined.

Liposomes have certain advantages over the solid core particles previously used, such as the ability to deliver imaging agents or biologically active drugs in their aqueous core or lipid bilayer. The coating of the liposomes can be designed to target a known surface receptor on TAMs increasing the prospect of cell uptake. TAMs have been shown in numerous human and mouse studies to overexpress surface scavenger receptors, such as the mannose receptor (CD206) [15–17], which is important for the clearance of mannose-bearing serum glycoproteins released at sites of inflammation and viruses, fungi, and bacteria [18,19]. We report herein a mannosylated liposome loaded with $^{64}$Cu for PET imaging of TAMs in a mouse model of lung cancer.

## 2. Materials and methods

### 2.1. Animal model

All experiments were carried out under protocols approved by the Institutional Animal Care and Use Committee. Our mouse model is based on one reported by Blackwell's group [20]. Female FVB mice (Jackson Laboratory, $n = 6$) aged 6e8 weeks received weekly intraperitoneal (IP) injections of 1 mg urethane/g body weight dissolved in sterile 0.9% NaCl. Control mice ($n = 3$) received saline IP injections. Twenty weeks after the initial

urethane injection, MRI was used to verify lung tumor presence. PET imaging was performed when at least one lung tumor reached 1.5 mm in diameter.

Prior to *in vivo* studies, we characterized macrophage infiltration at the tumor border in the urethane-FVB mouse model. Twenty-four weeks after urethane treatment, lungs from a representative mouse were harvested *en bloc* and inflated with formalin through the trachea. After formalin fixation, the lungs were embedded in paraffin, cut into 2 μm slices, and hematoxylin and eosin (H&E)-stained. Slides were digitized and examined for tumors.

To evaluate TAM density relative to macrophage density in normal lung, we immunostained lung sections ($n = 4$ urethane-treated mice) with rat anti-mouse F4/80 monoclonal antibody (AbDSerotec). F4/80 is a well-known, highly specific macrophage molecule in mice [21]. To estimate macrophage density, regions of interest (ROIs) were drawn in areas corresponding to stroma and normal lung. Macrophages were counted in areas of known size and macrophage density (MØ per square millimeter) was calculated. Ten ROIs were drawn in each compartment and the average density was computed.

Finally, we used confocal microscopy to estimate the percentage of F4/80 positive cells that overexpress CD206. Lungs ($n = 2$ mice, 24 weeks post-urethane) were harvested and inflated with 1.5 mL of Optimum Cutting Temperature (OCT; Fisher Scientific) through the trachea. The lungs were snap-frozen in liquid nitrogen, frozen into a block, and cryosectioned coronally. Frozen lung tissue sections were fixed and incubated with rat anti-mouse F4/80 and rabbit anti-mouse CD206 (AbDSerotec). After primary antibody incubation, sections were treated with Alexa Fluor 594-conjugated goat anti-rat IgG and Alexa Fluor 488-conjugated goat anti-rabbit IgG. Cell nuclei were visualized by 4′,6-diamidino-2-phenylindole (DAPI). Confocal images of tumor regions were captured using a fluorescence microscope (Carl Zeiss LSM 700). To estimate the percentage of cells within the tumor stroma that coexpress F4/80 and CD206, thresholding was applied to several images spanning different tumor regions across two mice.

## 2.2. Liposome preparation and characterization

Liposomes were composed of 18.8 mg/mL of L-a-Phosphatidylcholine, 4.2 mg/mL of cholesterol, and 0.025 mg/mL of the lipophilic fluorescent probe 3,3′-Dio-ctadecyloxacarbocyanine Perchlorate (DiO, $\lambda_{ex}$ = 484 nm, $\lambda_{em}$ = 501 nm, Molecular Probes, USA). The liposomes were made using dehydrationerehydration: the lipids and DiO were dissolved in chloroform, the solvent was evaporated, and the resultant thin-film hydrated with a 10 mM solution of chelating agent 1,4,7,10-tetra-azacyclododecane-1,4,7,10-tetraacetic acid (DOTA) in 10 mM 4-(2-Hydroxyethyl)-1-Piperazine-Ethanesulfonic Acid (HEPES) buffer with 150 mM NaCl and a pH of 4 for 2 h at 37 °C and overnight at 4 °C. The liposome solution was freeze-thawed 5 times and then extruded consecutively 20 times through 1 μm, 600 nm, 400 nm and 200 nm polycarbonate membrane filters using a Lipex extruder with high-pressure nitrogen. The non-encapsulated DOTA was removed by dialysis using a Slide-A-Lyzer G2 dialysis cassette with a molecular weight cut-off of 10,000 against five-2 L of HEPES buffer containing 150 mM NaCl (pH 7.4).

Mannosylated DOTA encapsulated liposomes (MAN-LIPs) were prepared as described above with the inclusion of neoglycolipids synthesized from mannotriose and dipalmitoylphosphatidylethanolamine (DPPE) by reductive amination (manufactured to our specification by Encapsula NanoSciences, Nashville, TN). The mannosylated phospholipid was added at a 1:20 MANeDPPE to phosphatidylcholine (PC) molar ratio and dissolved in chloroform. The mean particle diameter was verified by a laser light scattering particle size analyzer (LS-900, Otsuka Electronics). A schematic diagram of plain and MAN-LIPs is in Fig. 1.

### 2.3. $^{64}$Cu labeling

Remote loading was used to radiolabel DOTA-containing liposomes with the PET probe $^{64}$Cu ($t_{1/2}$ 12.7 h), by utilizing the lipophilic transporter hydroxyquinoline to ferry $^{64}$Cu to the liposome interior where it is more tightly chelated by the encapsulated DOTA [22]. Copper loading of the liposomes was confirmed using size exclusion chromatography (SEC) column to determine if the DiO labeled liposomes eluted in the same fractions as the radioactive $^{64}$Cu.

### 2.4. Culture of murine BMDM

To create primary macrophage cultures that mimic physiological and surface marker characteristics of macrophage phenotypes observed *in vivo*, bone marrow (BM) was flushed from the femurs and tibiae of FVB mice 8–12 weeks of age. The cell suspension was filtered using a 70-mm filter mesh, centrifuged at 500 × g, and resuspended in 1 mL of MACS buffer (phosphate buffered saline (PBS) supplemented with 1% bovine serum albumin (BSA) and 2 mM ethylenediaminetetraacetic acid). Four 10 cm polystyrene Petri plates were prepared with 8 mL complete media: α-Minimum Essential Medium (α-MEM; Gibco) supplemented with 10% heat-inactivated fetal bovine serum, 10% CMG14–12 cell conditioned medium (as a source of macrophage-colony stimulating factor (M-CSF)), and 1% pen/strep (complete α-MEM). The cell suspension was pipetted onto these Petri dishes and cultured 4 days at 37 °C with 5% $CO_2$ in a humidified chamber. This resulted in cells that were 95% positive for F4/80, consistent with other reported results [23]. After the 4 day incubation, adherent cells were treated for 10 min at 37 °C with 1 mL of trypsin (Gibco) diluted 1:10 in PBS. Recovered cells were counted using a hemacytometer and re-plated in 60 mm Petri dishes with 3 mL complete α-MEM at a density of $1.0 \times 10^6$ cells per well. 24 h after re-plating, the dishes were divided and treated for 24 h hours with either mouse recombinant interferon-g (IFN-g; PeproTech, Rocky Hill, NJ, 20 ng/mL) and lipopolysaccharide (LPS; SigmaeAldrich, 100 ng/mL) resulting in M1-like macrophages (M1–MØ), or mouse recombinant interleukin-4 (IL-4; PeproTech, Rocky Hill, NJ) plus IL-13 (PeproTech) at a concentration of 20 ng/mL each [24], resulting in M2-like macrophages (M2–MØ). *In vitro* stimulation of murine BM-derived macrophages with IL-4 and IL-13 has been shown to induce M2a or wound healing macrophages similar to TAMs [25]. Therefore, we used Western blot and flow cytometric analysis to assess mannose receptor expression to verify M2 polarization after cytokine treatment.

### 2.5. Evaluation of liposome uptake by MØ in vitro

Uptake of liposomes by macrophages was evaluated by flow cytometry (FACS-Calibur, BD Biosciences). M2–MØ and M1–MØ were incubated with either MAN or plain liposomes at a concentration of 960 nmol phospholipid per mL of PBS at 37 °C for 90 min. Cells that were incubated with PBS served as negative controls. Following incubation, the cells were washed three times in MACS buffer to remove non-associated liposomes and detached from the Petri dish with No-Zyme solution (Sigma). To measure cell surface mannose receptor expression, cells were incubated with anti-Fc receptor mAb for 60 min on ice to block non-specific binding of anti-body to the mouse Fcγ domain, then were incubated for 20 min with rat anti-mouse CD206 directly conjugated to Alexa Fluor 647 (AbD Serotec). The cells were then fixed with Cytofix (BD Biosciences) and transferred to flow tubes. Two-color flow cytometry was performed with 10,000 events acquired per sample. The fluorescent amplifiers of the FL-1 and FL-4 detector filters were adjusted to ensure that the negative cell population appeared in the first logarithmic decade. Compensation for spectral overlap was not required due to sufficient separation between the fluorescent emission profiles. All experiments were done in triplicate.

FlowJo (TreeStar Inc.) was used to analyze the raw flow data. Macrophages were identified by their light scattering properties. Using negative controls, cellular autofluorescence in both channels was determined by manually defining a gate that maximally included 1% of autofluorescent cells. Only cells exhibiting a fluorescence intensity above this gate were included in the analysis. CD206 expression was quantified in each treatment group as the geometric mean fluorescence intensity (MFI) of positive cells. Similarly, the geometric MFI of DiO fluorescence associated with M2–MØ and M1–MØ following liposome incubation was measured.

### 2.6. In vivo studies of liposome distribution and uptake by MØ

To determine the blood half-life of radiolabeled MAN and plain liposomes, repetitive tailevein bleeds (about 50 μL of blood per sample) were performed at 5 and 30 min, and 1.5, 3, 6, and 18 h after intravenous (IV) injection in 6 normal FVB mice. Liposome dose was 1.9 μmol total phospholipid labeled with 50–75 μCi (1.85–2.8 MBq) of $^{64}$Cu in a total volume of 160 μL. The radioactivity of each sample was measured using a γ-counter calibrated for $^{64}$Cu energy. In order to estimate how much radioactivity was in the total blood volume at each time point, we used a value of 7.3% of the body mass for total blood mass [26]. From this we calculated the percentage of the injected dose in total blood mass ($\%ID_{TBM}$) at each time point using:

$$\%ID_{TBM} = \frac{\left(\frac{\mu Ci_{sample}}{g_{sample}}\right) \times BW \times 0.073}{\mu Ci_{ID}} \quad (1)$$

where $\mu Ci_{sample}$, $g_{sample}$, $\mu Ci_{ID}$, and BW represents the radioactivity measured in the blood sample, the mass of the blood sample, the radioactivity of the injected dose (ID), and the body weight of the mouse, respectively.

24 weeks after urethane treatment, lung tumor bearing mice were IV injected with $^{64}$Cu-labeled MAN-LIPs via the lateral tail vein. Each mouse received 1.9 μmol total phospholipid labeled with 400–500 μCi (14.8e18.5 MBq) of $^{64}$Cu for a total volume of 160 μL. Mice were imaged using a Focus 120 PET scanner (Siemens, Knoxville, TN). During the 40 min PET acquisition, anesthesia was maintained using 1.25% isoflurane in $O_2$ inhaled through a nose cone. Heart rate, respiration, and rectal temperature were monitored (SAII, Stony Brook, NY). PET data were reconstructed using OSEM algorithm with 2 iterations and 12 subsets followed by MAP algorithm (18 iterations). The reconstructed image (not corrected for attenuation) was composed of 95 axial slices of thickness 0.79 mm with an in-plane voxel dimension of 0.4 mm × 0.4 mm (128 × 128 pixels). To determine the optimal time point after IV liposome injection for imaging, a preliminary study was conducted in which tumor to normal lung uptake ratios were computed on serial scans acquired over 18 h in 4 mice.

Immediately after the PET scan, MR images were acquired on a 4.7 T MRI system (Varian, Inc., Palo Alto, CA) to identify lung and tumor boundaries on the PET scans. MRI used a cardiac and respiratory gated multi-slice, spin-echo sequence developed in our lab with the following parameters: field of view = 25.6 mm, effective matrix = 128 × 128, slice thickness = 0.6 mm, TR = 168 ms, TE = 11 ms, number of averages = 4, number of slices = 10, and number of interleaves = 4, Gadolinium-DTPA (Magnevist; Bayer Schering Pharma, Berlin, Germany) was injected at a dose of 50 μmol/kg body weight in the hind leg muscle. The total scan time was 6–8 min per interleave, depending on the heart rate and breathing rate. Four 10-slice inter-leaved stacks were acquired to cover the entire lung field. To facilitate PET–MRI co-registration, a custom-designed multi-modality fusion phantom was scanned to determine the rigid-body transformation matrix for fusing subsequent mouse data sets.

Using AMIDE software [27], MAN-LIP uptake in tumor and remote lung tissue, liver, and muscle was quantified with PET using co-registered, resolution-matched MR images to guide the size and location of PET ROIs. For lung tumors, ROIs were carefully drawn around the tumor perimeter for each slice in which the tumor was visible. The percent injected activity per μL (%ID/μL) was computed for each tissue type by dividing the ROI-derived tissue tracer concentration by the radioactivity of the injected dose. Due to their small size, ROI-derived radioactivity concentration measurements in lung tumors suffer from partial volume effects (PVE). We corrected for PVE by multiplying the ROI-derived uptake concentration measured in the tumor by a recovery coefficient (RC) that was obtained using a hot-rod phantom containing a known radioactivity concentration. The phantom images allowed us to construct a look-up table that allows an RC value to be estimated based on the diameter of the object (tumor). Using MRI, we measured the average diameter for each lung tumor and assigned to it an RC value that was used to correct the ROI-derived radioactivity concentration.

### 2.7. Ex vivo tissue imaging

Immediately following imaging, the animals were euthanized and the lungs, liver, and spleen were harvested. The lungs were inflated with 1.5 mL of formalin through the trachea, which was then tied off with a suture. Tissues were washed and rescanned by PET with the same parameters and acquisition time described above. The primary motivation for acquiring *ex*

*vivo* PET scans was to image the lungs without the presence of signal contamination originating from the liver. Fluorescence imaging of the harvested organs was also performed using the IVIS Spectrum to examine the tissue distribution of DiO and its correlation with $^{64}$Cu. For DiO fluorescence imaging, we used an excitation filter centered at 500 nm and an emission filter centered at 540 nm. The lamp level was set to high, binning to medium, field of view to 6.4–12.3 cm depending on object size, *f* number to 2, and exposure time to 0.5–1 s such that no saturation occurred in the image.

Two representative mice that were administered MAN-LIPs were chosen for further analysis by confocal fluorescence microscopy. For this study, lungs were harvested after *in vivo* imaging and inflated with 1.5 mL of OCT via the trachea and snap frozen in liquid nitrogen. The lung tissue was then mounted in OCT embedding compound and stored at −80 °C until cut into 4 mm slices. Tumor-positive frozen tissue sections were fixed and incubated with rat anti-mouse F4/80 followed by Alexa Fluor 594-conjugated goat anti-rat IgG. For visualization of cell nuclei, slides were counterstained with DAPI. Each fluorophore was carefully selected to minimize spectral overlap and potential bleed-through artifacts. Immunofluorescent staining of frozen lung tissue was done by IHC Tech (Boulder, CO). All slides were analyzed using a Zeiss LSM 700 confocal scanning microscope.

### 2.8. Co-injection study

Even though the incorporation of mannotriose into liposome formulations has been shown to enhance macrophage uptake over plain liposomes both *in vitro* and *in vivo* [28–30], we set out to determine the significance of liposome mannosylation for targeting TAMs *in vivo* in our urethane animal model. The first study, intended to address the importance of liposome mannosylation in mediating uptake by TAMs, involved the co-injection of MAN and plain liposomes (Fig. 1) into lung tumor-bearing mice. The second study was identical to the first, with the exception that the plain liposomes were prepared with the inclusion of polyethyleneglycol (PEG)-bearing lipids at a molar ratio of 1:20 with respect to PC. The intent of this study is to find out what property is more critical for TAM targeting *in vivo* by IV injection: the inclusion of PEG which promotes long blood circulation time and retention at the tumor site due to the Enhanced Permeability and Retention effect, or the inclusion of mannose which may mediate enhanced liposome recognition and endocytosis. In order to independently detect each liposome type based on fluorescence, MAN-LIPs were prepared and labeled with DiO. However, plain liposomes (with and without PEG) were labeled with a red-shifted lipophilic dye (1,1′-Dioctadecyl-3,3,3′ ,3′-Tet-ramethylindodicarbocyanine (DiD), $\lambda_{ex}$ = 648 nm, $\lambda_{em}$ = 670 nm, Molecular Probes, USA) whose excitation/emission profile did not overlap with DiO.

For these *in vivo* studies, each mouse was tailevein injected with 1.9 μmol total phospholipid (approximately 80 μL) of each liposome type plus 80 mL of HEPES buffer for a total injected volume of 240 μL. 6 h after injection, the mice were euthanized and their lungs, liver, and spleen were harvested. Lungs were inflated with 1.5 mL of OCT via the trachea and carefully arranged on black construction paper along with the liver and spleen. Fluorescent images were acquired using the IVIS Spectrum system. Radiant efficiency for DiO and DiD, defined as the emission light detected (photons/sec/cm$^2$/str) normalized by the

illumination power density (μW/cm$^2$) was measured using the Living Image 4.0 (Xenogen Corp., Alameda, CA). Tumor-to-remote lung, tumor-to-liver, and tumor-to-spleen ratios were computed in mice co-injected with MAN-LIPs and plain liposomes ($n = 2$) and MAN-LIPs and PEG liposomes ($n = 2$).

In addition to whole lung *ex vivo* fluorescence imaging, we also investigated liposome uptake by TAMs at the cellular level. Immediately after imaging, lungs were snap frozen and stored at −80 °C until cut into 4 μm slices. Select tumor-positive tissue sections were further stained with DAPI and rat anti-mouse F4/80 followed by TRITC-conjugated goat anti-rat IgG. Confocal microscopy was used to examine the relative presence of MAN versus plain liposomes and MAN versus plain PEG liposomes within TAMs.

### 2.9. Statistical analysis

For comparison of the expression of CD206 and liposome association by macrophage treatment groups *in vitro*, a two-tailed unpaired Student's *t*-test was used for evaluating statistical significance. All data shown are representative of at least 3 independent experiments. The same statistical test was also used to compare tumor to remote lung liposome uptake measured from PET images and macrophage densities in different tissue compartments measured from immunohistochemistry images. *P* values were considered to be statistically significant when less than 0.05.

## 3. Results

### 3.1. Validation of urethane model

Twenty-four weeks after urethane treatment, lung tumors were clearly visible on H&E-stained tissue. The majority of tumors were located on the lung pleural surface, an observation consistent with other studies [31]. Quantification of F4/80-positive cells on immunohistochemistry images revealed that tumor stroma had a seven-fold higher macrophage density compared to remote lung (673 ± 196 vs. 89 ± 29 MØ/mm$^2$). It is interesting to note that there was no statistically significant difference between remote lung macrophage density in tumor-bearing mice (89 ± 29 MØ/mm$^2$) and macrophage density in lung tissue of saline-treated mice (85 ± 29 MØ/mm$^2$). This result suggests that lung tumors do not influence macrophage density in remote lung compared to that of normal lung in aged-matched, saline-treated mice.

Fig. 2 shows two contiguous lung sections stained in two different ways. The first section (Fig. 2A) was H&E stained which allowed clear identification of tumor and immune cell infiltration in the surrounding stroma. The second section underwent double-immunofluorescence staining to allow simultaneous visualization of F4/80 and CD206 expression in H&E-confirmed tumor areas. Individual color channels of the confocal image, spatially corresponding to the area in the H&E-stained image indicated by the black dashed box, are shown in Fig. 2B. Consistent with immunohistochemical analysis, there was moderate accumulation of F4/80 macrophages at the tumor border and significantly fewer macrophages within the tumor. At the border of the tumor (indicated by the dashed white line), the majority of F4/80 positive macrophages (red) also stain positive for CD206

(green), signifying an M2 macrophage phenotype consistent with other reported studies based on a similar urethane model [16,32].

To estimate the percentage of F4/80-positive cells that co-express CD206, we used a thresholding technique based on staining intensity. For both the red (F4/80) and the green (CD206) channels, cells were identified and the percent of cells that were positive for both F4/80-positive and CD206-positive cells was computed. After pooling together the results from all images, we estimate that 94% of $F4/80^+$ also stain for CD206, indicating that a great majority of macrophages in the tumor stroma are M2-like.

### 3.2. Liposome characterization

Successful conjugation of MAN with DPPE (MANeDPPE) was confirmed by MALDI-TOF mass spectrometry. The *m/z* spectrum demonstrated a strong peak at 1180.6 for the protonated molecule consistent with the theoretical mass value of 1180.7. As determined by laser light scattering, liposomes exhibited a Gaussian size distribution with the peak of the Gaussian curve aligning with the pore size of the membrane (200 nm). The majority of the extruded population was between 180 and 220 nm.

The remote labeling of liposomes by the PET radionuclide $^{64}Cu$ was verified by SEC. The chromatography profile revealed that the peak of $^{64}Cu$ elution aligned with the peak of fluorescence (DiO) elution, confirming that $^{64}Cu$ was entrapped in the liposomes upon exiting the column. The elution of free $^{64}Cu$ alone occurred much later when passed through the column separately. Nearly 100% of the starting radioactivity was recovered in the void volume and was associated with the liposome fractions.

### 3.3. In vivo liposome uptake

We measured mannose receptor expression in the cultured macrophages. CD206 expression was upregulated on M2–MØ compared to M1–MØ as measured by flow cytometry and Western blotting, respectively. The uptake of plain and MAN-LIPs by M1–MØ and M2–MØ was assessed by flow cytometry. Following identification based on scatter properties, macrophages were analyzed for DiO fluorescence. Fluorescence histograms of M1–MØ and M2–MØ following a 90 min incubation with either DiO-labeled plain or MAN liposomes showed that MAN-LIPs were more strongly associated with macrophages of both stimulation groups compared to plain liposomes. However, quantification of the flow cytometry data revealed a significant 1.9-fold higher association of MANeLIPs with M2–MØ compared to M1–MØ ($P < 0.05$). This enhanced association is likely due to receptor recognition of liposome mannotriose and subsequent mannose receptor-mediated endocytosis.

### 3.4. In vivo studies

The blood clearance of $^{64}Cu$ labeled liposomes was studied in normal healthy FVB mice after administration of 10 MBq of radio-labeled liposomes through the lateral tail vein. The blood clearance of both liposomes followed a monoexponential decay with half-lives of 0.33 and 0.23 h for MAN-LIPs and plain liposomes, respectively. This result is consistent with previously published work which measured a blood half-life of less than 30 min for

liposomes of similar size and composition (PC and cholesterol) [33]. Examples of coronally acquired spin-echo MRI of a urethane and saline-treated mouse are shown in Fig. 3. Several tumors are clearly visible in the lungs of the urethane-treated mouse, which are easily detected relative to normal lung tissue which is nearly void of signal. In contrast, the saline-treated mouse has no detectable lung tumors.

To assess *in vivo* TAM targeting, $^{64}$Cu-labled MAN-LIPs were IV injected into lung tumor-confirmed mice ($n$ 6). PET imaging was performed 6 h following injection. This time point was chosen because it resulted in the highest $^{64}$Cu signal ratio between tumor tissue and remote lung while still maintaining sufficiently high radioactivity counts. Furthermore, after 6 h approximately 1% of the injected dose remains in the blood circulation, minimizing potential signal contamination from $^{64}$Cu-MAN-LIPs that may reside in the vasculature.

Fig. 4A shows a coronal MRI revealing a tumor in the right lung (white arrow) and a PET image (Fig. 4B) showing the distribution of MAN-LIPs 6 h post injection. Fused data sets (Fig. 4C) confirm high tumor localization of the PET signal compared to normal lung tissue. Following the *in vivo* scans, the lungs were excised and imaged by PET without the spillover from the nearby liver. The distribution of DiO-labeled liposomes within the excised lung was evaluated by fluorescence imaging acquired using the IVIS Spectrum. This information could not be obtained *in vivo* due to limited tissue penetration and photon scattering. A photo of the excised lung clearly shows the tumor (arrow, Fig. 4D) as well as several other smaller tumors. The fluorescence image overlaid on the photo reveals a strong DiO-fluorescent signal within the tumor and minimal accumulation in non-tumor areas of the lung (Fig. 4E). E*x vivo* PET maximum intensity projection image, shown in Fig. 4F, shows focal $^{64}$Cu signal in the area of the lung spatially corresponding to the tumor and the fluorescence signal as shown in Fig. 4D–E.

The average diameter of lung tumors measured across all mice studied ranged from 1.25 mm to 2.65 mm. This corresponded to RC values of 0.32–0.72. The PV-corrected uptake of $^{64}$Cu-labeled MAN-LIPs in lung tumors was 9.62 ± 2.49 %ID/μL at 6 h post injection. In contrast, uptake in normal lung tissue was significantly lower (1.4 ± 0.6 %ID/μL) resulting in a tumor-to-normal lung ratio of 6.7.

Following PET imaging, the dual-labeled MAN-liposome permitted a detailed assessment of cellular distribution by confocal fluorescence microscopy within lung tumor tissue. As shown in Fig. 5A, significant DiO fluorescence was associated with F4/80-positive cells (TAMs). (In this image, the tumor was not captured in the field of view but was located immediately to the right.) Furthermore, this fluorescence was not limited to the circumference of TAMs, but rather was clustered within them as clearly seen on the enlarged view of the TAM (Fig. 5B) indicated by the yellow arrow. This clustered distribution of DiO fluorescence is consistent with liposome entrapment in endosomal structures, signifying that tumor enhanced *in vivo* PET signals were the result of MAN-liposome-labeled TAMs.

### 3.5. Co-injection results

In order to accurately assess liposome lung distribution following co-injection, we first demonstrated that the fluorescence associated with each liposome type could be separately

detected. Using our equipment, the fluorescent dye DiO could be excited and detected apart from DiD using an excitation and emission filter pair of 500 nm and 540 nm, respectively. Conversely, DiD could be detected apart from DiO using an excitation and emission filter pair of 605 nm and 640 nm, respectively. This was expected based on their non-overlapping excitation and emission spectra.

Representative *ex vivo* fluorescence images of lungs 6 h after the co-injection of MAN and plain liposomes as well as MAN and PEG liposomes are shown in Fig. 6A, and 6B, respectively. From these images it was clearly evident that MAN and plain liposomes strongly localized at lung tumors. However, MAN liposomes exhibited a lower background signal in non-tumor lung tissue. PEG liposomes showed a diffuse lung distribution and consequently poor tumor contrast likely due to their enhanced blood circulation time.

To examine uptake in various tissues, we computed uptake ratios between the tumor and remote lung, tumor and liver, and tumor and spleen for each liposome type based on the fluorescence images. Tissue ratios were computed to avoid potential biases in the excitation of the fluorescent dyes as well as to avoid biases due to differences in signal attenuation in animal tissues. As shown in Fig. 7A, MAN-LIPs exhibited a higher tumor-to-remote lung (4.6) and tumor-to-spleen (3.7) ratio compared to plain liposomes. However, the tumor-to-liver ratio was comparable (0.8). MAN-LIPs also exhibited a high tumor-to-remote lung ratio (1.4) when co-injected with PEG liposomes. PEG liposomes exhibited the lowest tumor-to-remote lung ratio (0.9) of the three liposomes studied. This is likely due to the slow rate of blood clearance of these liposomes which results in a strong background signal, particularly in the well-vascularized tissue of the lung. For the MAN-LIPs, the tumor-to-remote lung ratio was 2.4 times larger than plain, and 4.9 times higher than PEG liposomes. This is largely due to the rapid clearance of the MAN-LIPs from normal lung. The uptake by TAMs and rapid clearance from normal surrounding tissue is an important property for using the MAN-LIPs as a TAMs imaging agent.

## 4. Discussion

Recent evidence has highlighted the role of macrophages, particularly of the M2 subtype, in the malignant progression of lung tumors. This recognition has spurred considerable effort to establish techniques to quantitatively monitor TAMs through noninvasive imaging. It has been previously shown that incorporating mannosylated phospholipids into liposomes improves targeting to peritoneal macrophages *in vivo* by receptor-mediated endocytosis [28,34]. This approach for monitoring TAMs by PET imaging has two significant advantages over fluorescently-labeled iron oxide nanoparticles designed for detection by MRI and optical techniques. First, the targeted liposomes are radiolabeled and thus can be tracked using PET imaging, which possesses a higher intrinsic sensitivity ($10^{-8}$ to $10^{-9}$ mol/L for PET compared to $10^{-3}$ to $10^{-5}$ mol/L for MRI). Second, liposomes provide a flexible platform for delivering both hydrophobic and hydrophilic cargo. For this study the aqueous interior core of liposomes was utilized to encapsulate a hydrophilic chelating agent to allow for remote labeling of the PET radionuclide, $^{64}$Cu. This compartment of the liposome also could be used to encapsulate a wide array of hydrophilic drugs including cytotoxic agents that abolish TAMs through apoptosis or immunomodulatory agents that

could trigger their reversal from a pro-tumoral M2 phenotype to a tumoricidal M1 phenotype. For example, it was recently shown that the cytokine IFN-γ induced human TAMs to switch from immunosuppressive to immunostimulatory phenotype [35].

Results from our *in vitro* studies revealed a significantly higher association of MAN-LIPs with M2–MØ compared with plain liposomes. Furthermore, M2–MØ exhibited significantly higher uptake of MAN-LIPs compared to M1–MØ, correlating with CD206 expression on these cells. Interestingly, M1–MØ exhibited a preference for MAN-LIPs over plain liposomes in spite of their low expression of CD206. This result may be explained by a study that found that IFN-γ enhances mannose receptor-mediated phagocytosis, despite its effects on surface mannose receptor down-regulation [36]. More studies are needed to determine what receptors are responsible for the uptake of MAN-LIPs by M1–MØ and also if this uptake behavior occurs *in vivo*.

PET images showed enhanced MAN-LIPs signal in regions corresponding with lung tumors compared to areas of remote lung at 6 h post injection. Due to the small size of the lung tumors, we used a look-up table approach to estimate the RC value for each lung tumor in order to correct for PVE. We acknowledge some limitations to this approach. First, we did not account for radioactivity “spill-in” of surrounding tissue into tumor ROIs. We believe that the size of the lesion is the primary determinant of the RC, with background activity influencing it only to a small degree. This has been demonstrated by other groups with phantom experiments [37]. Furthermore, as shown by *in vivo* and *ex vivo* PET images of the same lung, ROI-derived radioactivity concentrations of lung tumors were not significantly affected by their proximity to the liver. Another limitation of this approach is that we do not respiratory gated the PET images which can result in image blurring particularly in the thoracic region. Studies in mice have shown that non-respiratory gated PET imaging can lead to significant tumor standardized uptake value underestimations depending on lesion size [38]. However, a gated PET acquisition typically suffers from a reduced signal-to-noise ratio compared to a non-gated one and because of this we chose not to employ it.

There were distinct differences between MAN and plain-liposomes in lung distribution following their co-injection. The fluorescence signal of plain liposomes was significantly higher than that of MAN-LIPs in areas of lung absent of visible tumors. This finding is likely not due to tissue autofluorescence because DiD excitation occurs within a range of wavelengths where tissue autofluorescence is minimal. A possible explanation for the elevated remote lung signal is a delayed lung clearance of plain liposomes compared to MAN-LIPs. However, this is not likely since their measured blood clearance half-lives were nearly identical. Another possible explanation for this behavior could be due to an increased uptake of plain liposomes by resident alveolar macrophages. While this explanation is not consistent with other studies that have demonstrated enhanced targeting to alveolar macrophages by mannose-coated liposomes after intratracheal administration in rats [29] and IV administration in mice [39], it is unknown if lung tumors influence the phagocytic behavior of these cells. Lastly, the complement system is a major factor in the clearance of liposomes [40]. Additional studies would be needed to determine whether plain liposomes more efficiently activate complement, which could promote better recognition by alveolar macrophages and lead to higher lung sequestration. A flow cytometry study could be

designed to help determine if lung resident macrophages are responsible for uptake or if the delayed lung clearance of plain liposomes is due to mechanisms not related to cellular uptake.

Our results obtained from confocal microscopy verified that macrophages were responsible for the elevated fluorescence signal observed within the areas of lung tumors on whole-lung fluorescent images. Microscopy revealed that all three liposome types were internalized by TAMs. The whole-lung fluorescence images of PEG-LIPs did not reveal high TME to background contrast due to the slow rate of clearance of these liposomes from the blood and prominent signal throughout the lung. These findings are significant because they indicate that MAN-LIPs, which are rapidly cleared from the blood relative to PEG liposomes, are able to target lung TAMs and that a slow rate of blood clearance is not required for targeting these cells. Rapid blood clearance and effective targeting are attractive properties of MAN-LIPs and highlight their potential use as TAM imaging and/or delivery agents. Our data show that MAN-LIPs not only demonstrated targeting of TAMs, but also rapid clearance in normal lung which is critical for achieving high tumor contrast by PET imaging.

## 5. Conclusions

The influence of TAMs on tumor growth has been shown by numerous groups to be dependent on their differentiation state. In this paper we demonstrated the successful targeting of mannosylated liposomes to TAMs in a mouse model of pulmonary adenocarcinoma. Confocal microscopy verified that the PET signal was due to liposome internalization by TAMs. Although co-injection studies revealed that plain and PEG liposomes are both internalized by TAMs, MAN-LIPs exhibited the highest tumor to remote lung ratios on whole-lung fluorescent images showing that it is a promising agent for the localized delivery of imaging and potentially other agents to the tumor microenvironment.

## Acknowledgments

The work was supported in part by a gift provided to the University of Virginia by Philip Morris USA (PMUSA). The review and approval process was overseen by an External Advisory Committee without any affiliation with the University, PMUSA, or any other tobacco company. PMUSA funding for this work to SSB was based upon independent intramural and extramural reviews. The sponsor did not have any role in the study design, in the collection, analysis and interpretation of data, in the writing of the report, nor in the decision to submit the paper for publication. The work was also supported by an National Institute of Health grant awarded to MWM (R01CA104397).

## References

[1]. Marin L, Colombo P, Bebawy M, Young PM, Traini D, Marin L, et al. Chronic obstructive pulmonary disease: patho-physiology, current methods of treatment and the potential for simvastatin in disease management. Expert Opin Drug Deliv 2011;8(9):1205–20. [PubMed: 21615218]

[2]. Murphy BS, Bush HM, Sun dareshan V, Davis C, Hagadone J, Cory TJ, et al. Characterization of macrophage activation states in patients with cystic fibrosis. J Cyst Fibros 2010;9(5):314–22. [PubMed: 20570573]

[3]. Allavena P, Sica A, Solinas G, Porta C, Mantovani A, Allavena P, et al. The inflammatory micro-environment in tumor progression: the role of tumor-associated macrophages. Crit Rev Oncol Hematol 2008;66(1):1–9. [PubMed: 17913510]

[4]. Bingle L, Brown NJ, Lewis CE, Bingle L, Brown NJ, Lewis CE. The role of tumour-associated macrophages in tumour progression: implications for new anti-cancer therapies. J Pathol 2002;196(3):254–65. [PubMed: 11857487]

[5]. Murdoch C, Muthana M, Coffelt SB, Lewis CE, Murdoch C, Muthana M, et al. The role of myeloid cells in the promotion of tumour angiogenesis. Nat Rev Cancer 2008;8(8):618–31. [PubMed: 18633355]

[6]. Siveen KS, Kuttan G, Siveen KS, Kuttan G. Role of macrophages in tumour progression. Immunol Lett 2009;123(2):97–102. [PubMed: 19428556]

[7]. Robinson SC, Scott KA, Wilson JL, Thompson RG, Proudfoot AE, Balkwill FR, et al. A chemokine receptor antagonist inhibits experimental breast tumor growth. Cancer Res 2003;63(23):8360–5. [PubMed: 14678997]

[8]. Zeisberger SM, Odermatt B, Marty C, Zehnder-Fjallman AH, Ballmer-Hofer K, Schwendener RA, et al. Clodronate-liposome-mediated depletion of tumour-associated macrophages: a new and highly effective antiangiogenic therapy approach. Br J Cancer 2006;95(3):272–81. [PubMed: 16832418]

[9]. Banciu M, Metselaar JM, Schiffelers RM, Storm G, Banciu M, Metselaar JM, et al. Antitumor activity of liposomal prednisolone phosphate depends on the presence of functional tumor-associated macrophages in tumor tissue. Neoplasia 2008;10(2):108–17. [PubMed: 18283332]

[10]. Zhang B, Yao G, Zhang Y, Gao J, Yang B, Rao Z, et al. M2-polarized tumor-associated macrophages are associated with poor prognoses resulting from accelerated lymphangiogenesis in lung adenocarcinoma. Clinics (Sao Paulo) 2011;66(11):1879–86. [PubMed: 22086517]

[11]. Pollard JW, Pollard JW. Tumour-educated macrophages promote tumour progression and metastasis. Nat Rev Cancer 2004;4(1):71–8. [PubMed: 14708027]

[12]. Weissleder R, Kelly K, Sun EY, Shtatland T, Josephson L, Weissleder R, et al. Cell-specific targeting of nanoparticles by multivalent attachment of small molecules. Nat Biotechnol 2005;23(11):1418–23. [PubMed: 16244656]

[13]. Leimgruber A, Berger C, Cortez-Retamozo V, Etzrodt M, Newton AP, Waterman P, et al. Behavior of endogenous tumor-associated macrophages assessed in vivo using a functionalized nanoparticle. Neoplasia 2002;11(5): 459–68.

[14]. Melancon MP, Lu W, Huang Q, Thapa P, Zhou D, Ng C, et al. Targeted imaging of tumor-associated M2 macrophages using a macromolecular contrast agent PG-Gd-NIR813. Biomaterials 2010;31(25):6567–73. [PubMed: 20537382]

[15]. Allavena P, Chieppa M, Bianchi G, Solinas G, Fabbri M, Laskarin G, et al. Engagement of the mannose receptor by tumoral mucins activates an immune suppressive phenotype in human tumor-associated macrophages. Clin Dev Immunol 2010;2010:547179. [PubMed: 21331365]

[16]. Redente EF, Orlicky DJ, Bouchard RJ, Malkinson AM, Redente EF, Orlicky DJ, et al. Tumor signaling to the bone marrow changes the phenotype of mono-cytes and pulmonary macrophages during urethane-induced primary lung tumorigenesis in A/J mice. Am J Pathol 2007;170(2):693–708. [PubMed: 17255336]

[17]. Mantovani A, Sozzani S, Locati M, Allavena P, Sica A, Mantovani A, et al. Macrophage polarization: tumor-associated macrophages as a paradigm for polarized M2 mononuclear phagocytes. Trends Immunol 2002;23(11):549–55. [PubMed: 12401408]

[18]. Lee SJ, Evers S, Roeder D, Parlow AF, Risteli J, Risteli L, et al. Mannose receptor-mediated regulation of serum glycoprotein homeostasis. Science 2002; 295(5561):1898–901. [PubMed: 11884756]

[19]. McGreal EP, Martinez-Pomares L, Gordon S, McGreal EP, Martinez-Pomares L, Gordon S. Divergent roles for C-type lectins expressed by cells of the innate immune system. Mol Immunol 2004;41(11):1109–21. [PubMed: 15476922]

[20]. Stathopoulos GT, Sherrill TP, Cheng DS, Scoggins RM, Han W, Polosukhin VV, et al. Epithelial NF-kappaB activation promotes urethane-induced lung carcinogenesis. Proc Natl Acad Sci U S A 2007;104(47):18514–9. [PubMed: 18000061]

[21]. Austyn JM, Gordon S, Austyn JM, Gordon S. F4/80, a monoclonal antibody directed specifically against the mouse macrophage. Eur J Immunol 1981; 11(10):805–15. [PubMed: 7308288]

[22]. Petersen AL, Binderup T, Rasmussen P, Henriksen JR, Elema DR, Kjaer A, et al. 64Cu loaded liposomes as positron emission tomography imaging agents. Biomaterials 2011;32(9):2334–41. [PubMed: 21216003]

[23]. Yamazaki T, Nagata K, Kobayashi Y, Yamazaki T, Nagata K, Kobayashi Y. Cytokine production by M-CSF-and GM-CSF-induced mouse bone marrow-derived macrophages upon coculturing with late apoptotic cells. Cell Immunol 2008;251(2):124–30. [PubMed: 18511028]

[24]. Kigerl KA, Gensel JC, Ankeny DP, Alexander JK, Donnelly DJ, Popovich PG, et al. Identification of two distinct macrophage subsets with divergent effects causing either neurotoxicity or regeneration in the injured mouse spinal cord. J Neurosci 2009;29(43):13435–44. [PubMed: 19864556]

[25]. Mosser DM, Edwards JP, Mosser DM, Edwards JP. Exploring the full spectrum of macrophage activation. Nat Rev Immunol 2008;8(12):958–69. [PubMed: 19029990]

[26]. Litzinger DC, Huang L, Litzinger DC, Huang L. Amphipathic poly(ethylene glycol) 5000-stabilized dioleoylphosphatidylethanolamine liposomes accumulate in spleen. Biochim Biophys Acta 1992;1127(3):249–54. [PubMed: 1511002]

[27]. Loening AM, Gambhir SS, Loening AM, Gambhir SS. AMIDE: a free software tool for multimodality medical image analysis. Mol Imaging 2003;2(3):131–7. [PubMed: 14649056]

[28]. Matsui M, Shimizu Y, Kodera Y, Kondo E, Ikehara Y, Nakanishi H, et al. Targeted delivery of oligomannose-coated liposome to the omental micrometastasis by peritoneal macrophages from patients with gastric cancer. Cancer Sci 2010;101(7):1670–7. [PubMed: 20507320]

[29]. Wijagkanalan W, Higuchi Y, Kawakami S, Teshima M, Sasaki H, Hashida M, et al. Enhanced anti-inflammation of inhaled dexamethasone palmitate using mannosylated liposomes in an endotoxin-induced lung inflammation model. Mol Pharmacol 2008;74(5):1183–92. [PubMed: 18669445]

[30]. Wijagkanalan W, Kawakami S, Takenaga M, Igarashi R, Yamashita F, Hashida M, et al. Efficient targeting to alveolar macrophages by intratracheal administration of mannosylated liposomes in rats. J Control Release 2008; 125(2):121–30. [PubMed: 18037185]

[31]. Bauer AK, Cho HY, Miller-Degraff L, Walker C, Helms K, Fostel J, et al. Targeted deletion of Nrf2 reduces urethane-induced lung tumor development in mice. PLoS ONE 2011;6(10): –26590.

[32]. Redente EF, Dwyer-Nield LD, Merrick DT, Raina K, Agarwal R, Pao W, et al. Tumor progression stage and anatomical site regulate tumor-associated macrophage and bone marrow-derived monocyte polarization. Am J Pathol 2010;176(6):2972–85. [PubMed: 20431028]

[33]. Shimkin MB, Stoner GD, Shimkin MB, Stoner GD. Lung tumors in mice: application to carcinogenesis bioassay. Adv Cancer Res 1975;21:1–58. [PubMed: 1108612]

[34]. Kojima N, Biao L, Nakayama T, Ishii M, Ikehara Y, Tsujimura K, et al. Oligomannose-coated liposomes as a therapeutic antigen-delivery and an adjuvant vehicle for induction of in vivo tumor immunity. J Control Release 2008; 129(1):26–32. [PubMed: 18485512]

[35]. Duluc D, Corvaisier M, Blanchard S, Catala L, Descamps P, Gamelin E, et al. Interferon-gamma reverses the immunosuppressive and protumoral properties and prevents the generation of human tumor-associated macrophages. Int J Cancer 2009;125(2):367–73. [PubMed: 19378341]

[36]. Raveh D, Kruskal BA, Farland J, Ezekowitz RA, Raveh D, Kruskal BA, et al. Th1 and Th2 cytokines cooperate to stimulate mannose-receptor-mediated phagocytosis. J Leukoc Biol 1998;64(1):108–13.

[37]. Srinivas SM, Dhurairaj T, Basu S, Bural G, Surti S, Alavi A, et al. A recovery coefficient method for partial volume correction of PET images. Ann Nucl Med 2009;23(4):341–8. [PubMed: 19367446]

[38]. Branco SS, Almeida P. Respiratory motion modeling in small animal PET using GATE. NSS ‘08. IEEE Nucl Sci Symp Conf Rec 2012; 2008.

[39]. Singodia D, Verma A, Verma RK, Mishra PR. Investigations into an alternate approach to target mannose receptors on macrophages using 4-sulfated N-acetyl galactosamine more efficiently in comparison with mannose-decorated liposomes: an application in drug delivery. Nanomed Nanotechnol Biol Med 2012;8(4):468–77.

[40]. Ishida T, Harashima H, Kiwada H, Ishida T, Harashima H, Kiwada H. Liposome clearance. Biosci Rep 2002;22(2):197–224. [PubMed: 12428901]

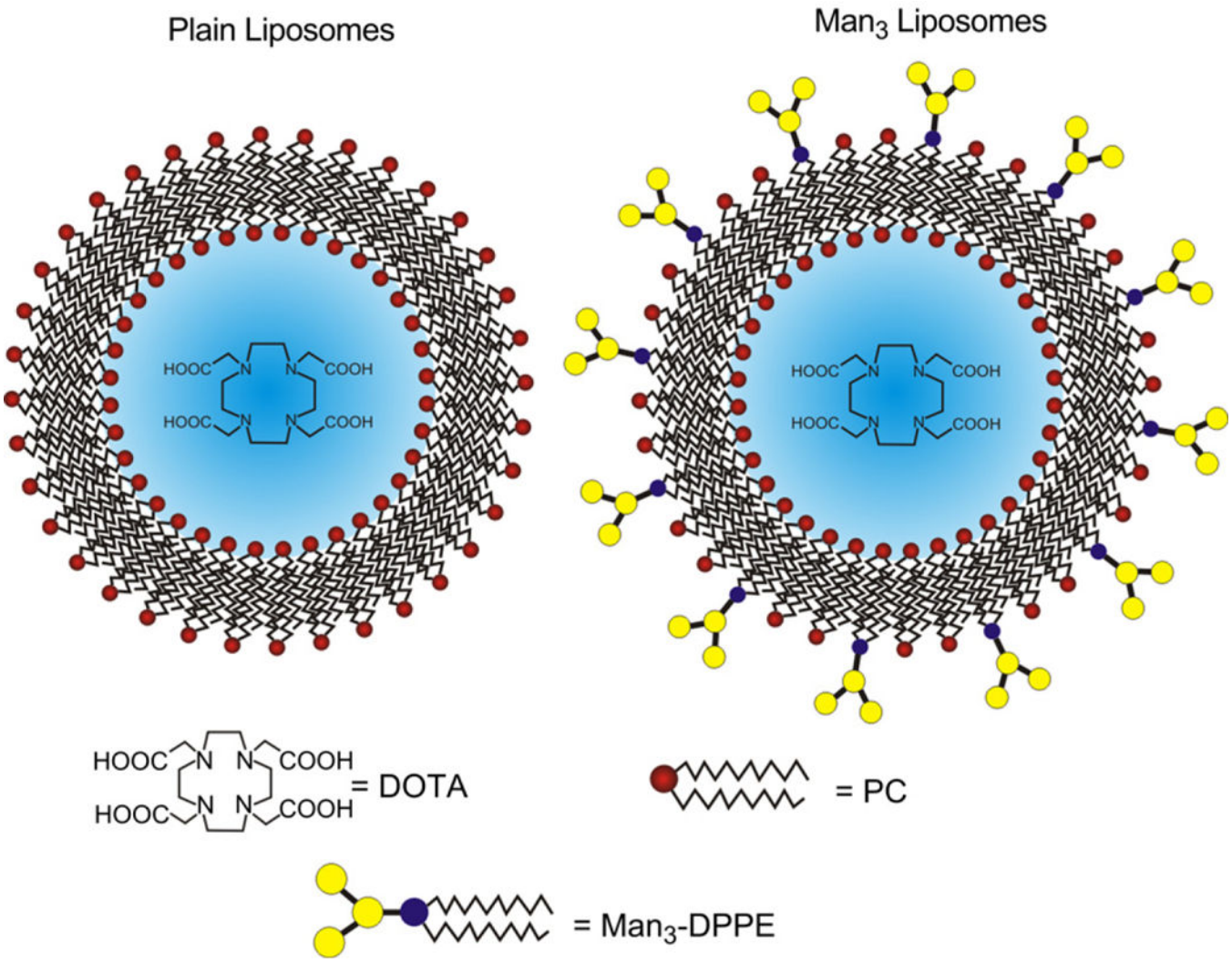


**Fig. 1.**

A schematic diagram of liposomes. DOTA-containing plain (left) and $Man_3$ (right) liposomes allow for remote loading of the PET imaging agent, $^{64}Cu$. The mean liposome diameter was 200 nm.

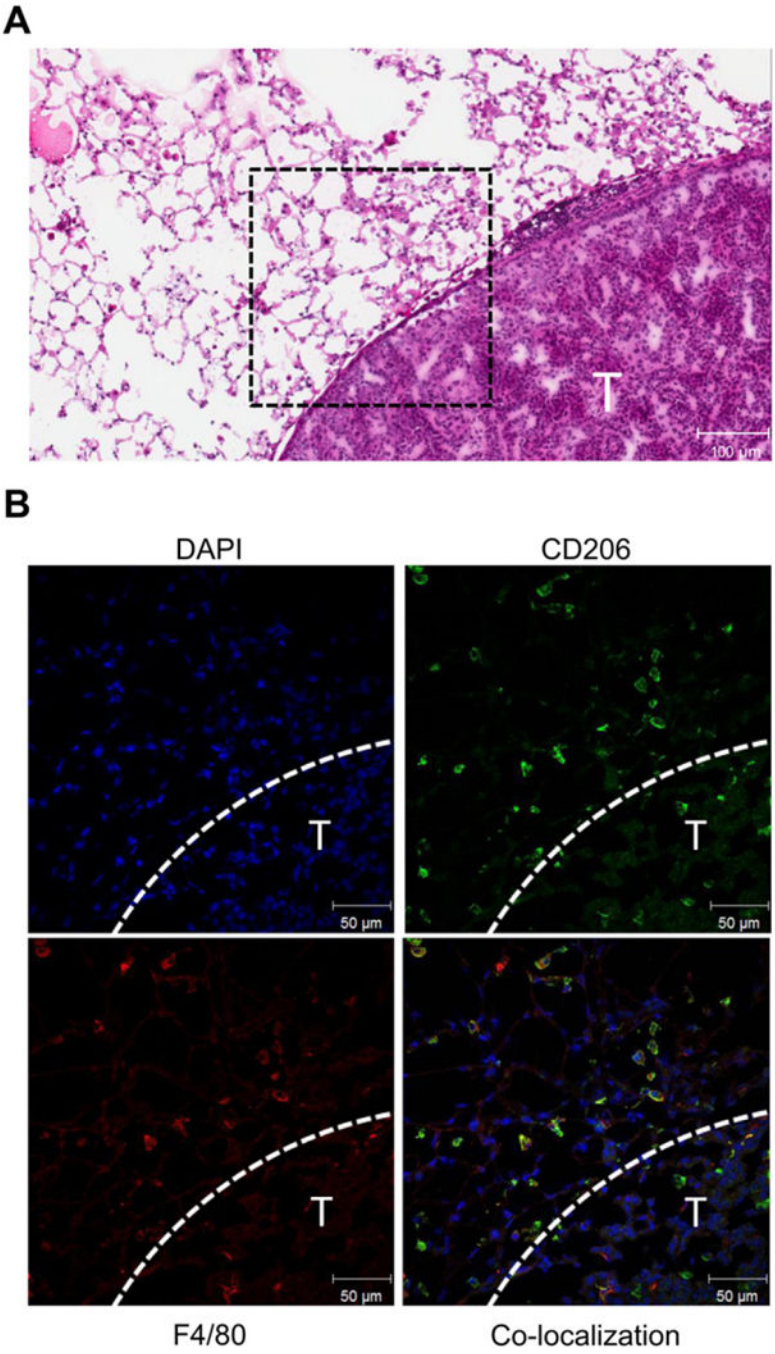


**Fig. 2.**

Macrophage M2 polarization in lungs of a urethane-treated mouse 25 weeks after treatment. The H&E image shows a tumor boundary (T) with moderate immune cell infiltration in the stroma (A). Immunofluorescence staining of the tumor stroma outlined in the H&E image by the black dashed box is shown in (B). At the edge of the tumor (indicated by dashed white line), the majority of macrophages identified by F4/80 (red) also stain for CD206 (green) indicating M2 polarization.(For interpretation of the references to colour in this figure legend,the reader is referred to the web version of this article.)

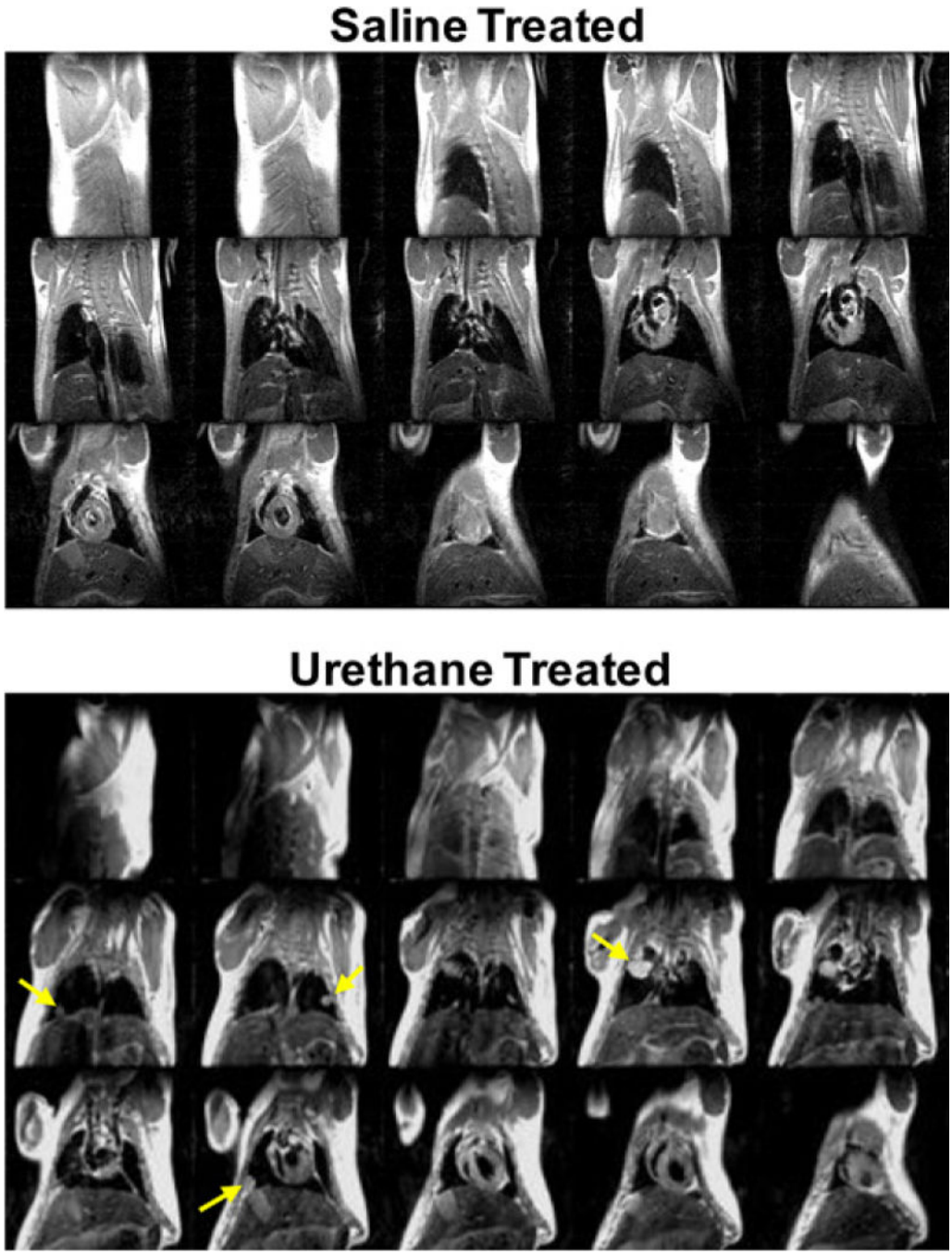


**Fig. 3.**

Representative spin echo MR images of a saline (top) and urethane-injected (bottom) mouse 24 weeks following treatment. These scans were acquired approximately 30 min after gadolinium injection. Lungs tumors, as indicated by yellow arrows, are clearly visible in the urethane-treated mouse. In contrast, no lung tumors are detected in the saline-treated mouse. (For interpretation of the references to colour in this figure legend, the reader is referred to the web version of this article.)

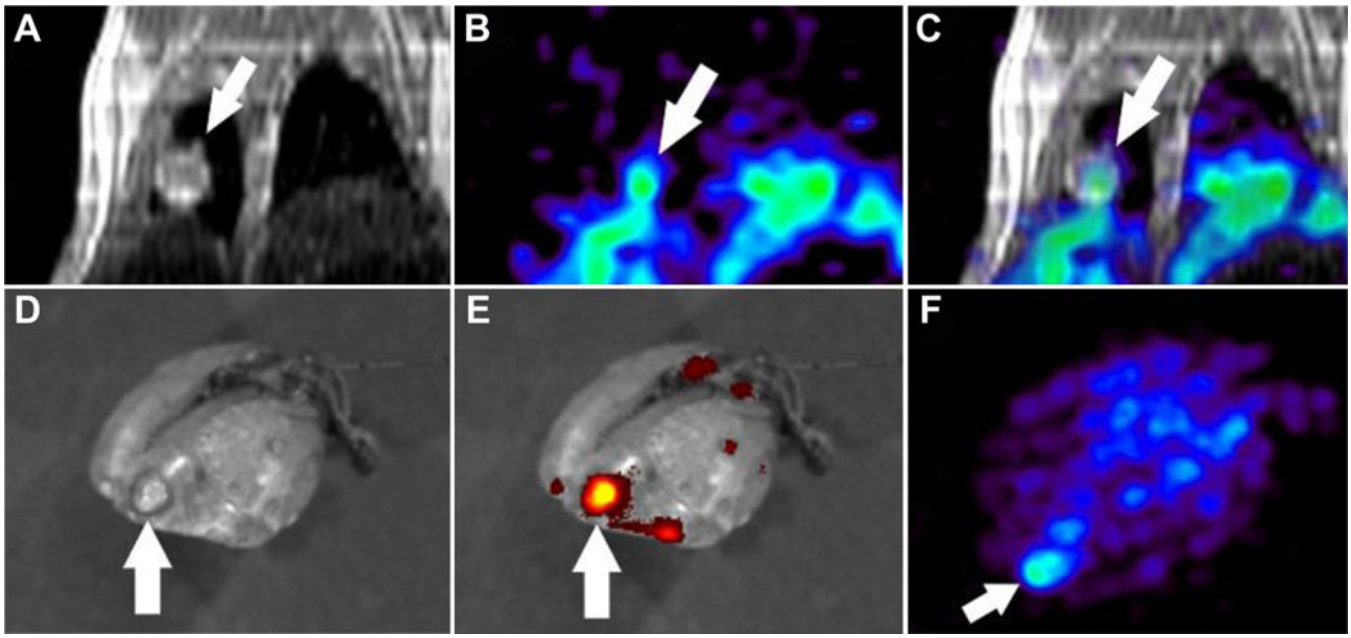


**Fig. 4.**

Representative *in vivo* images showing a lung tumor on coronal MRI (A) with enhanced $^{64}$Cu-labeled $Man_3$-liposome uptake on PET 6 h after i.v. injection (B). PET-MR image registration (C) verifies tumor localization of the PET signal. *Ex vivo* fluorescence image of the lung was obtained to assess DiO distribution. A photo shows the tumor (D) which exhibited higher DiO accumulation compared to non-tumor lung areas. *Ex vivo* PET maximum intensity projection image (F) showed focal $^{64}$Cu signal in the area of the lung spatially corresponding to the tumor shown in the photograph.

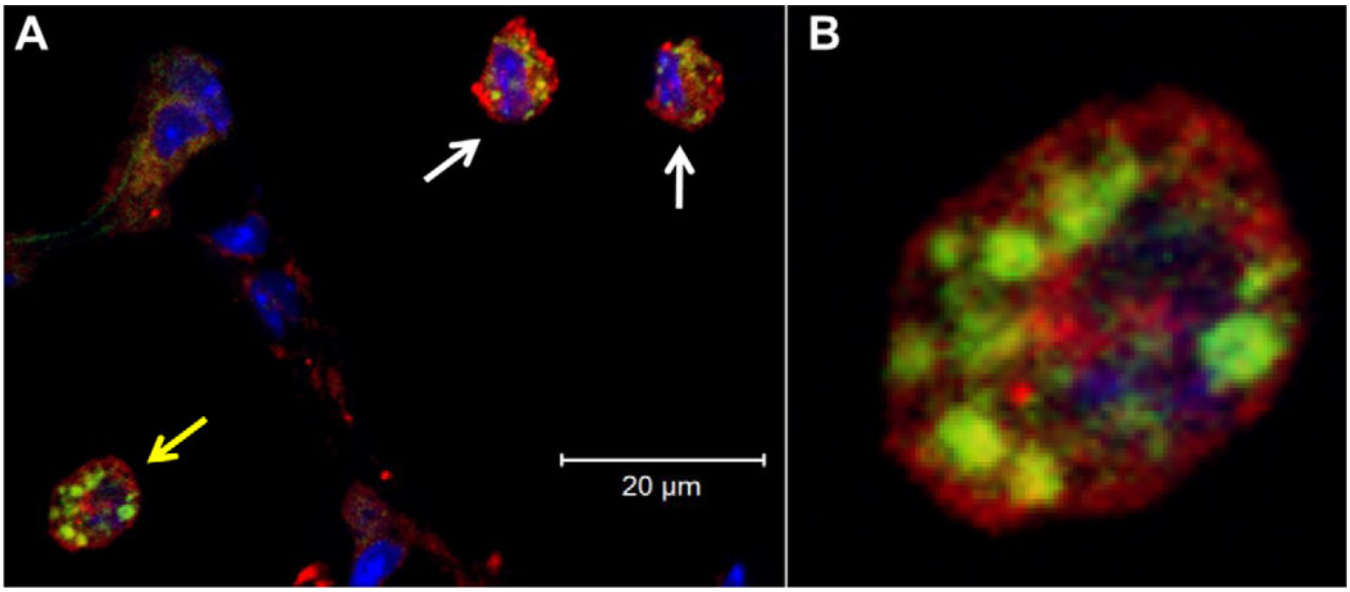


**Fig. 5.**

Confocal fluorescence microscopy revealed internalization of DiO-labeled $Man_3$-liposomes (green) by F4/80+ macrophages (red) within the tumor stroma 6 h after i.v. liposome injection. Cell nuclei are stained with DAPI (blue). (A) A co-localized confocal image shows the intracellular localization of $Man_3$-liposomes within TAMs. The enlarged view of the cell indicated by the yellow arrow is shown in (B), clearly shows a clustered distribution of liposomes consistent with storage in macrophage lysosomal structures. (For interpretation of the references to colour in this figure legend,the reader is referred to the web version of this article.)

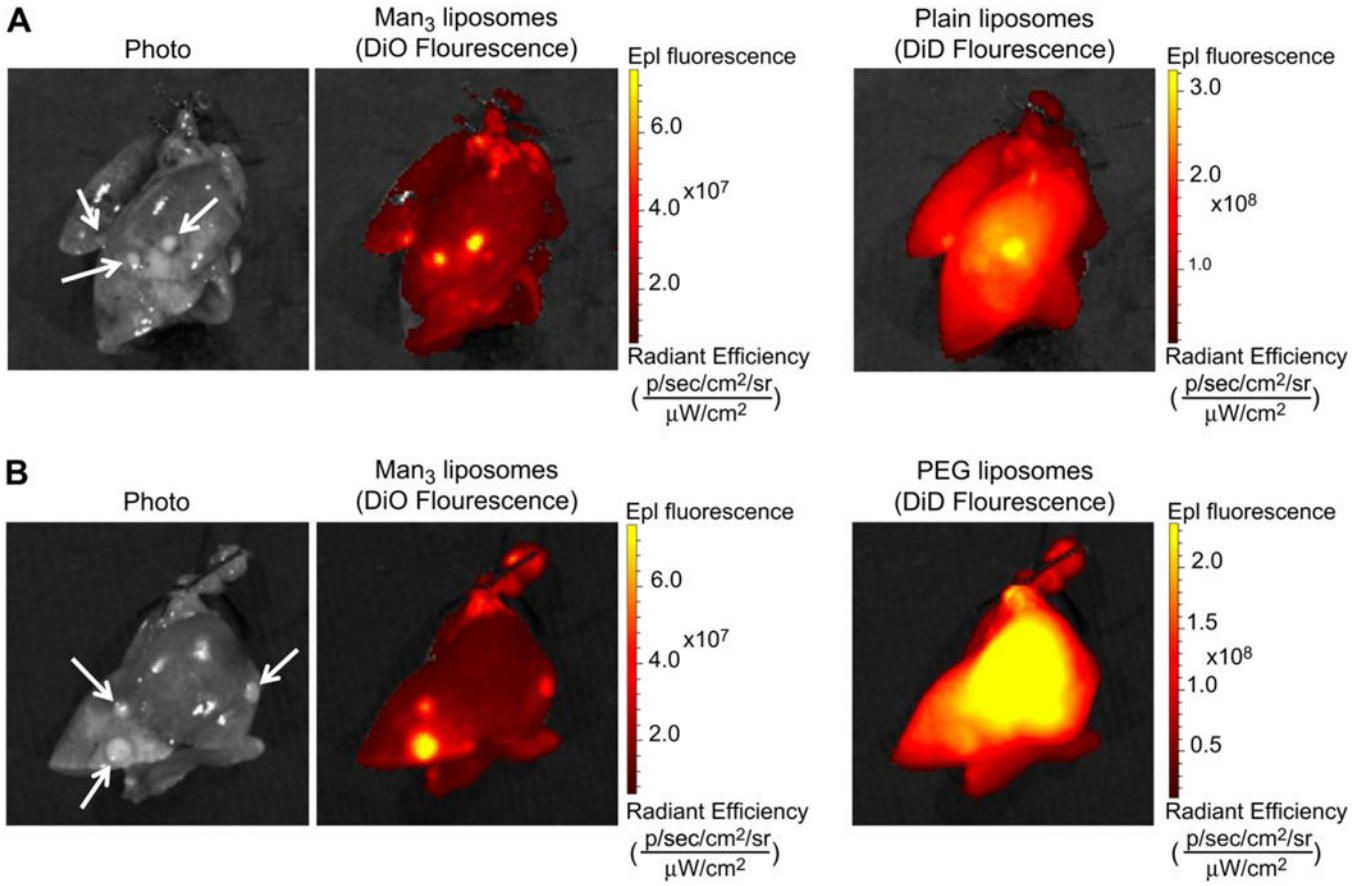


**Fig. 6.**

Representative photos and fluorescent images from the liposome co-injection study. Images of excised lungs 6 h after the co-injection of $Man_3$ and plain liposomes (A) and $Man_3$ and PEG liposomes (B). Strong fluorescence signal associated with $Man_3$ and plain liposomes is localized to lung tumors (identified by white arrows on the photo). However, compared to $Man_3$-liposomes, plain liposomes exhibit a higher background signal. PEG liposomes show a diffuse lung distribution and consequently poor tumor contrast likely due to their enhanced blood circulation time.

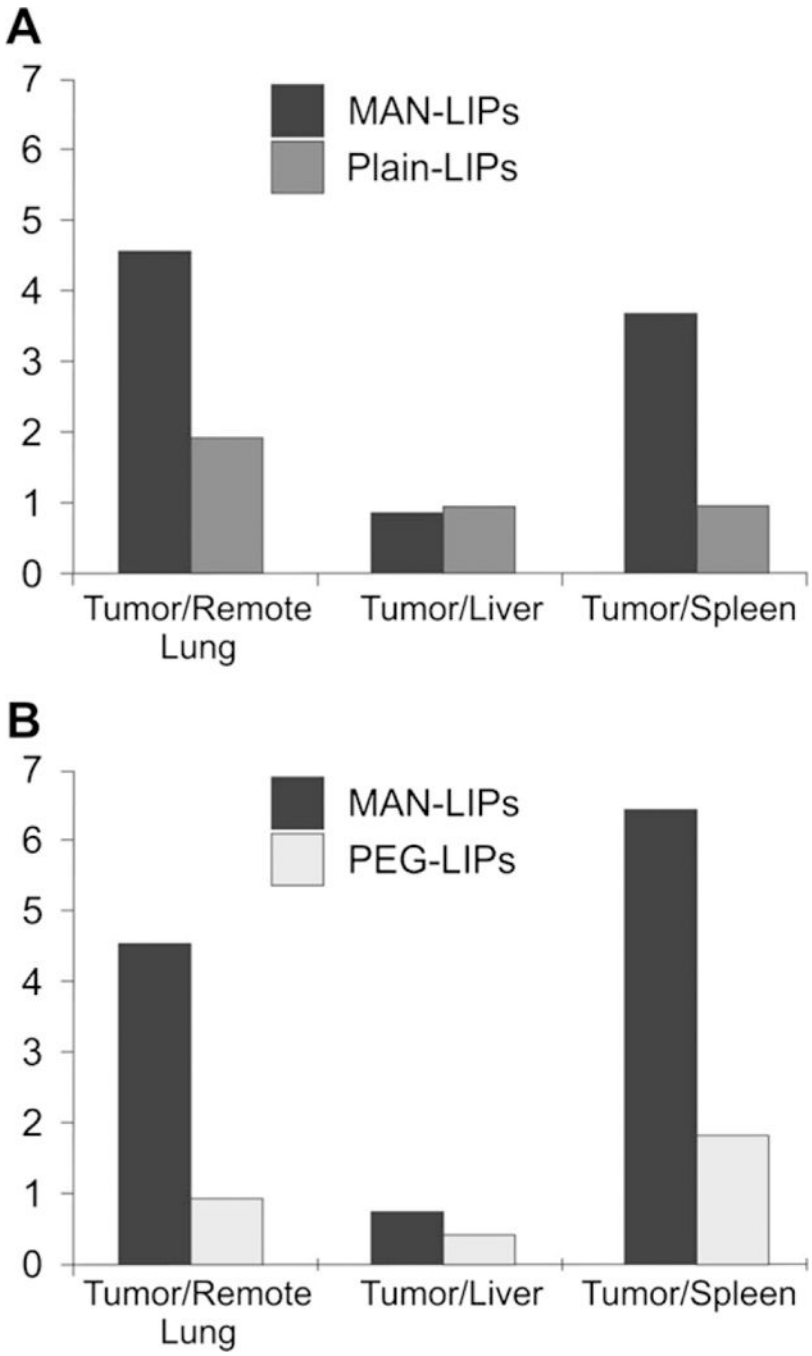


**Fig. 7.**

Tumor-to-tissue ratios measured from fluorescence images of harvested organs following the co-injection of MAN and plain liposomes (A) and MAN and PEG lipo-somes (B). MAN-LIPs exhibited a higher tumor-to-remote lung and tumor-to-spleen ratio compared to plain liposomes, while tumor-to-liver ratios were comparable. MAN-liposomes also exhibited a high tumor-to-remote lung ratio following co-injection with PEG liposomes, likely due to

the slow rate of blood clearance of PEG liposomes. PEG liposomes also showed a reduced tumor-to-liver ratio, consistent with a lower rate of capture by the RES.